Science

AAAS

Supplementary Materials for

Photo-induced chirality in a nonchiral crystal

Z. Zeng *et al*.

Corresponding author: A. Cavalleri, andrea.cavalleri@mpsd.mpg.de

The PDF file includes:

Materials and Methods
Supplementary Text
Figs. S1 to S8
Tables S1 to S5
References

Materials and Methods

1. Experimental Setup

The schematic of the pump-probe setup used in the experiment is shown in Figure S1. The THz excitation pulses were generated by difference frequency generation (DFG) in a GaSe crystal, using the two independently wavelength tunable near-infrared signal outputs of two optical parametric amplifiers (OPAs). The OPAs were seeded by the same white light and pumped by overall 1.5-mJ, 30-fs pulses at 800 nm wavelength from a 1-kHz repetition rate Ti:sapphire amplifier system. An off-axis parabolic mirror was used to focus the THz beam onto the sample with a ~70 μm FWHM spot size. The generated THz pulses were carrier-envelope-phase (CEP) stable and characterized by electro-optical sampling in a second GaSe crystal at the sample position (*36*).

The probe pulses for the polarization rotation measurements in the BPO_4 (001) single crystal were sourced by the same amplifier system and focused onto the sample with a lens to a ~30 μm spot. Polarization control of the probe incident on the sample was achieved using a quarter waveplate and a polarizer. Its pump-induced polarization rotation was measured using a combination of a half waveplate, a Wollaston prism and two photodiodes.

The pump and probe beams were aligned collinear and at normal incidence to the sample surface. Two identical narrow bandpass filters (center wavelength at 808 nm and bandwidth of 5 nm) were employed before and after the sample to filter out high-frequency components in the time-resolved response induced by the Pockels effect, which, in contrast to the light-induced birefringence and the light-induced optical activity, generates sidebands to the incident probe spectrum. The THz excitation pulses were linearly polarized along the *a*- or *b*- axis of the *c*-axis oriented BPO_4 crystal. All the measurements were carried out at room temperature.

2. Sample Preparation and Characterization

Polycrystalline BPO_4 powder was synthesized with high-purity H_3BO_3 (99.9995%) and $NH_4H_2PO_4$ (99.998%) powders, before being ground, pelletized, and sintered. Single crystals were grown from this powder using Li_2MoO_4 flux via the top-seeded solution growth technique in a platinum crucible at up to 975°C. After homogenization, the melt was slowly cooled down, resulting in the growth of high-quality BPO_4 single crystals.

These crystals were characterized by x-ray diffractometry and oriented with an optically flat (001) surface using focused ion beam milling. Xenon ions were accelerated at 30 kV at a beam current of 2.5 mA for the surface orientation. To reduce roughness, the sample was finally milled at grazing incidence with a beam current of 200 nA (*37*). The thickness of the sample used in this experiment was ~200 μm.

The static optical properties in the THz frequency range were characterized by Fourier-transform infrared reflectivity (FTIR) measurements, with the light electric field polarized along the *a*-axis. Figure S3 clearly shows all the four E-symmetry phonon modes of BPO_4 in the detected spectrum, which was fitted with the following dielectric function for phonons (*38*).

$$\varepsilon(\omega) = \varepsilon_\infty + \varepsilon_\infty \sum_j \frac{\omega_{LO,j}^2 - \omega_{TO,j}^2}{\omega_{TO,j}^2 - \omega^2 - i\omega\gamma_j}$$

The fitting results are listed in Table S1. In the experiments reported here, we resonantly excited the E(2) mode.

Supplementary Text

1. Analysis of the Time-resolved Polarization Rotation Measurements

In the time-resolved experiments, the probe pulses propagate along the optical axis of the crystal (*c*-axis), polarized in the *a-b* plane. Hence, the permittivity tensor elements along crystal *a*- and *b*-axis are considered as follows.

Due to the $\bar{4}$ symmetry of BPO$_4$, the static permittivity is isotropic in the *a-b* plane:

$$\boldsymbol{\varepsilon} = \begin{pmatrix} \varepsilon_{11} & 0 \\ 0 & \varepsilon_{22} \end{pmatrix} = \begin{pmatrix} \varepsilon_{11} & 0 \\ 0 & \varepsilon_{11} \end{pmatrix}.$$

Based on a symmetry analysis, and as confirmed by our ab-initio calculations, the atomic displacements along the B-symmetry phonon modes induce both, optical activity and birefringence, at the same time. It is important to note that the birefringence potentially caused by a Kerr effect shares the same symmetry as that induced by B-mode displacements. The permittivity tensor taking into account the birefringence is symmetric and follows the form

$$\boldsymbol{\varepsilon}' = \begin{pmatrix} \varepsilon_{11} + \Delta\varepsilon_{11} & \Delta\varepsilon_{12} \\ \Delta\varepsilon_{12} & \varepsilon_{11} - \Delta\varepsilon_{11} \end{pmatrix}.$$

By rotating the coordinate frame around the *c*-axis, the permittivity can be diagonalized as

$$\boldsymbol{\varepsilon}'' = \begin{pmatrix} \varepsilon_{11} - b & 0 \\ 0 & \varepsilon_{11} + b \end{pmatrix},$$

where $b = \sqrt{\Delta\varepsilon_{11}^2 + \Delta\varepsilon_{12}^2}$.

The optical activity tensor element g_{33} introduces additional imaginary antisymmetric components into the permittivity tensor

$$\Delta\varepsilon_{ij}(\omega) = i\, l_{ijk} g_{kl}(\omega) k_l(\omega)$$

where l_{ijk} is levi-civita symbol, k is the wavevector, ω is the angular frequency.

The probe, polarized in the a-b plane, is sensitive to the permittivity within the same plane, specifically to g_{33}, which is zero in the ground state due to the system's $\bar{4}$ symmetry. However, the B-mode distortion enables g_{33} to become non-zero, altering the permittivity to the following form:

2

$$\boldsymbol{\varepsilon'''} = \begin{pmatrix} \varepsilon_{11} - b & ic \\ -ic & \varepsilon_{11} + b \end{pmatrix},$$

where coefficient c is the effective optical activity and b is the effective birefringence.

Due to the finite extinction depth δ of the THz-frequency excitation pulses, the light-induced changes in permittivity decay exponentially, resulting in a depth-dependent non-equilibrium permittivity tensor

$$\boldsymbol{\varepsilon'''}(z) = \begin{pmatrix} \varepsilon_{11} - b(0) \times e^{-\frac{z}{\delta}} & ic(0) \times e^{-\frac{z}{\delta}} \\ -ic(0) \times e^{-\frac{z}{\delta}} & \varepsilon_{11} + b(0) \times e^{-\frac{z}{\delta}} \end{pmatrix},$$

where $b(0)$ and $c(0)$ are the changes in permittivity at the surface $z = 0$.

Since the 5-mm penetration depth of the 808-nm probe pulses is much larger than the sample thickness, the measured polarization rotation signal accumulates when the optical probe propagates through the sample.

We employed the following Jones matrix analysis to differentiate between the signal contributions from the time-dependent optical activity and birefringence(*39*). At equilibrium, the crystal is isotropic, and the probe pulses remain linearly polarized as they propagate in the sample. For each incident probe polarization, the half waveplate behind the sample is rotated to balance the intensity on the two photodiodes in the absence of the pump.

The excitation pulses change the permittivity as described above. The incident linearly polarized probe pulse can be decomposed into two eigenvectors following the permittivity tensor in the pumped state described above. Defining $f = \frac{c(0)}{b(0)}$, the eigenvectors in the *a-b* plane are two elliptically polarized light waves with opposite ellipticity.

$$\boldsymbol{e_1} = \begin{pmatrix} \dfrac{i(-1+\sqrt{1+f^2})}{f\sqrt{1+\frac{(-1+\sqrt{1+f^2})^2}{f^2}}} \\[3em] \dfrac{1}{\sqrt{1+\frac{(-1+\sqrt{1+f^2})^2}{f^2}}} \end{pmatrix} \qquad \boldsymbol{e_2} = \begin{pmatrix} \dfrac{-i(1+\sqrt{1+f^2})}{f\sqrt{1+\frac{(1+\sqrt{1+f^2})^2}{f^2}}} \\[3em] \dfrac{1}{\sqrt{1+\frac{(1+\sqrt{1+f^2})^2}{f^2}}} \end{pmatrix}$$

We note that the decay of the strength of the light-induced state over the extinction depth δ does not change the eigenvectors themselves, but only the difference in the splitting in the refractive indices (see Fig. S4A).

The effective refractive indices for the two eigenvectors are

$$n_1 = \sqrt{\varepsilon_{11} + \sqrt{b(z)^2 + c(z)^2}}$$

$$n_2 = \sqrt{\varepsilon_{11} - \sqrt{b(z)^2 + c(z)^2}}.$$

The phase delay between the two eigenvectors increases with propagation length, with a rate proportional to the difference in refractive index.

$$\frac{d\gamma}{dz} = \frac{2\pi}{\lambda_0}(n_1 - n_2)$$

Since the light-induced change in the effective refractive indices is small compared to the static refractive index ($\sqrt{b^2 + c^2} \ll n_0$),

$$\frac{d\gamma}{dz} \approx \frac{1}{\lambda_0} 2\pi \left(\left(n_0 + \frac{\sqrt{b^2 + c^2}}{2n_0} \right) - \left(n_0 - \frac{\sqrt{b^2 + c^2}}{2n_0} \right) \right) = \frac{1}{\lambda_0} 2\pi \frac{\sqrt{b^2 + c^2}}{n_0}.$$

Integrating over the entire sample thickness d, we acquire the phase difference between the two eigenvectors (see also Fig. S4B)

$$\gamma = \int_0^d \frac{1}{\lambda_0} 2\pi \frac{\sqrt{b^2 + c^2}}{2n_0} dx = \frac{\delta}{\lambda_0} 2\pi \frac{\sqrt{b(0)^2 + c(0)^2}}{n_0} \left(1 - e^{-\frac{d}{\delta}} \right).$$

The two eigenvectors are then recombined after exiting the sample. The beam passes through the half waveplate and is split onto the two detectors, intensity balanced in the absence of the pump. The polarization rotation signal is proportional to the normalized difference between the intensities on the two detectors

$$\theta(\varphi) = \frac{I_1 - I_2}{2(I_1 + I_2)} = \frac{1}{2\sqrt{1 + 1/f^2}} \sin(\gamma) + \frac{(\cos(\gamma) - 1)}{4(1 + f^2)} \sin(4\varphi - \phi).$$

Here, φ is the incoming polarization angle relative to the pump and ϕ is the relative angle between the pump to the optical axis of the transient birefringent state. For phase differences $\gamma \ll 1$, we approximate $\sin(\gamma) \approx \gamma$ and $\cos(\gamma) \approx 1 - \frac{\gamma^2}{2}$ and find

$$\theta(\varphi) = \frac{\pi\delta \left(1 - e^{-\frac{d}{\delta}} \right)}{\lambda_0 n_0} c(0) - \frac{\pi^2 \delta^2 \left(1 - e^{-\frac{d}{\delta}} \right)^2}{2\lambda_0^2 n_0^2} \sin(4\varphi) b(0)^2.$$

It is clearly seen here that the signal is composed of two contributions. The first one is proportional to the optical activity coefficient $c(0)$ and does not depend on the incoming probe polarization.

The second contribution is proportional to the square of the birefringence coefficient $b(0)^2$ and depends on the incoming probe polarization with a $90°$-periodicity, as observed in the experiments. The average of the birefringence contribution over all the incident probe polarizations is zero.

Hence, the pure optical activity c is proportional to the average value of the polarization rotation signal over all the incoming polarization of the probe pulse. The pump-induced polarization rotation $\theta(\varphi)$ is fitted with the above expression at each time delay. The fitting result of the experimental data shown in Fig. 3B of the main text is plotted in Figure S5.

The rotary power ρ is defined as being proportional to the optical activity coefficient c, with

$$\rho = \frac{\pi c}{\lambda_0 n_0}.$$

The birefringence-induced difference in refractive index shown in Figure 3B & 3E of the main text follows

$$\Delta n = \frac{2\pi\, b}{\lambda_0 n_0}.$$

The light-induced time-dependent rotary power, extracted from our experiments as described above and shown in Figures 3C and 3E of the main text, was then fitted by the functions of the following form, which is a product of a step function with finite rise time σ and an exponential decay with decay time τ, reflecting the excitation and decay of the optical phonons by the THz-frequency excitation pulse.

$$\theta(t) = A\left(\text{erf}\left(\frac{t - t_0}{\sigma}\right) + 1\right) * e^{-\frac{t}{\tau}}.$$

Figure S6 illustrates the contribution to polarization rotation signal from birefringence. When a linearly polarized pulse passes through a birefringent crystal, the outgoing beam becomes elliptically polarized. The projection on the *x*- and *y*-axes (the balancing axes for the incoming polarization) will differ depending on the relative angle between the incoming polarization and the fast axis of the birefringent material. The resulting signal exhibits a four-fold symmetry with respect to the incoming polarization.

2. Symmetry Analysis of the Nonlinear Phonon Coupling

Following Neumann's principle, the nonlinear coupling between phonons must be totally symmetric under all operation elements of the point group crystal class (10). For BPO4 with point group symmetry $\bar{4}$, the lowest order coupling to the B-symmetry phonon modes is given by

$$U = \alpha\left(Q_{Ey}^2 - Q_{Ex}^2\right)Q_B + \beta Q_{Ex}Q_{Ey}Q_B.$$

In the experiment, we selectively excited only one of the two doubly degenerate E modes at a time, thus the last coupling term with the coefficient β is not considered.

We note that in the $\bar{4}$ point group system, E-symmetry modes also drive the system into a transient chiral state (Table S4). However, due to the two-fold rotation symmetry, all the odd-order coupling terms between E-symmetry modes (such as Q_{Ex}^3 or $Q_{Ex}^2 Q_{Ey}$) are not allowed, prohibiting any rectified displacement of the crystal lattice along the E-symmetry modes. Therefore, the transient chirality can only be induced by the rectified displacement in the B-symmetry modes.

3. Density Functional Theory Calculations

We performed first-principles calculations in the framework of density functional theory (DFT) to explore the phonon excitation spectrum, the anharmonic lattice coupling coefficients, and the optical response of BPO_4 within the following technical and numerical settings.

In general, we used the Vienna Ab-initio Simulation Package (VASP) 6.2 DFT implementation (40-42) and the Phonopy software package (43) for the phonon calculations. Our computations utilized pseudopotentials generated within the Projector Augmented Wave (PAW) method (44). Specifically, we took the configured default pseudopotentials for B $2s^2 2p^1$, P $3s^2 3p^3$, and O $2s^2 2p^4$ potentials and applied the Local Density Approximation (LDA) for the exchange-correlation potential. As the final numerical setting, after convergence checks, we used a 7x7x5 Monkhorst-Pack (45) generated k-point mesh sampling of the Brillouin zone and a plane-wave energy cutoff of 600 eV for the calculations of structural relaxation and phonons. We re-iterated self-consistent calculations until the change in total energy converged up to 10^{-8} eV. All the phonon mode and anharmonic coupling constant computations were performed in a 2x2x2 conventional cell of BPO_4. All the calculations of the mode effective charge and the dielectric response, including the optical activity, were performed within the LOPTICS settings of VASP, in addition to the approaches utilized in References (46, 47). In order to achieve convergence for the optical properties, we had to increase the k-point mesh to 17x17x11 points and increased the number of empty states to 400.

The starting point of our first-principles investigation is the tetragonal cell of BPO_4. First, we determined the DFT equilibrium volume for this cell, which is $V_{cell} = 122.8$ Å^3 ($a = b = 4.30$ Å, $c = 6.62$ Å). We found the atomic equilibrium positions at the following Wyckoff positions B 2d, P 2a and O 8g (0.259,0.141,0.127). We then calculated the relevant phonon eigenfrequencies and eigenvectors at the Brillouin zone center, and their respective coupling constants defined in Supplementary Section S5. We list the relevant data in Table S2.

We also computed the changes in the symmetric and antisymmetric parts of the dielectric tensor arising from the lattice distortions along the coordinates of the four transiently displaced B-symmetry modes and the directly driven mode E(2). We list the changes in the optical permittivity ε arising from the associated birefringence and optical activity in Table S3 and S4.

4. Simulation of the nonlinear phonon dynamics and the transient physical properties

We used the equations of motions, introduced as Eqs. (1) and (2) in the main text, to calculate the crystal lattice dynamics induced by the resonant optical excitation of the doubly-degenerate mode E(2) at about 19 THz frequency. The starting point for all the phonon parameters of this procedure were the first-principles calculations described in Supplementary Section S5.

6

The left panels of Fig. S7 shows these dynamics for the excitation with the optical pump polarized along the crystal a-axis. Fig. S7A plots the THz electric field with center frequency of 19 THz and peak field of 5 MV/cm. Fig. S7B plots the oscillations of the resonantly driven E-symmetry phonon $Q_{E,a}$ polarized along the *a-axis*. Fig. S7C depicts the response of all the four nonlinearly coupled B-symmetry modes that are rectified due to the force, which is quadratic in the amplitude of $Q_{E,a}$ (see Eq.(2) of the main text). Fig. S7D & S7E show the changes of the birefringence and the optical activity, respectively, arising from the combined rectified motion of all the B-symmetry modes and using the data presented in Table S3. Fig. S7F to S7J show the equivalent data set for the optical excitation along the crystal b-axis. These data sets allowed us to simulate the time-delay dependent changes in the optical properties shown in Figure 3 of the main text.

Lastly, we also explore a quantified measure of chirality by similar to the approach developed in a recent study (*25*). We define a geometric chirality order parameter as

$$\vec{C} = \frac{1}{N} \sum \vec{r_j} \times \vec{d_{ji}} \quad ,$$

where $\vec{r_j}$ runs over the central sites (B and P), and $\vec{d_{ji}}$ corresponds to the bond direction vector to its neighboring oxygen atoms. In this definition a system is chiral if $|\vec{C}| > 0$. The projection of $\vec{C}$ onto the principal axis allows to determine the amount of left- or right-handedness of the structure. In Fig. S7F & S7M, we show how this measure changes as a function of time, where positive and negative signs correspond to right- or left-handedness, respectively. Note, that besides this geometric measure also other possible order parameters for chirality exists, such as the electric toroidal monopole (*24,48*).

Lastly, we note that the rectified displacement of the B modes also induces a transient electric polarization along the c-axis. We can estimate the magnitude of this polarization from our simulations by associating each B-mode displacement with its characteristic mode effective charge. We find that this polarization reaches a magnitude of approximately 0.1 μC/cm², and its time dependence is illustrated in Figs. S7G and S7N.

5. Definition of Antiferro-chiral Systems

The term 'antiferro-chiral' has been previously used in the literature to describe racemic crystals, comprising equivalent ratios of chiral fragments, for example molecules with opposite handedness (*5*). Here, based on symmetry arguments, we provide a general and rigorous definition applicable to both molecular and crystalline systems.

Antiferro-chiral crystalline systems are defined as those achiral systems, which possess at least one vibrational mode that induces chirality in the system. These systems have the potential to form a chiral lattice structure under external stimuli that couple linearly to such vibrational modes.
In crystalline (solid state) systems, materials of different symmetries can be categorized into the 32 crystallographic point groups. For each of the 21 achiral point groups, there exists at least one irreducible representation (irrep) that induces chirality in the system (see Table S5). However, the presence of a phonon mode with such symmetry depends on the specific crystal structure. Hence, only those achiral systems, which host at least one such mode, are antiferro-chiral. The relationship

of the classification is shown in Figure S8. It is important to note the following properties of antiferro-chiral.

- Antiferro-chirality is not an intrinsic property of a point group or a space group.
- Antiferro-chirality exists in both, centrosymmetric and non-centrosymmetric systems.
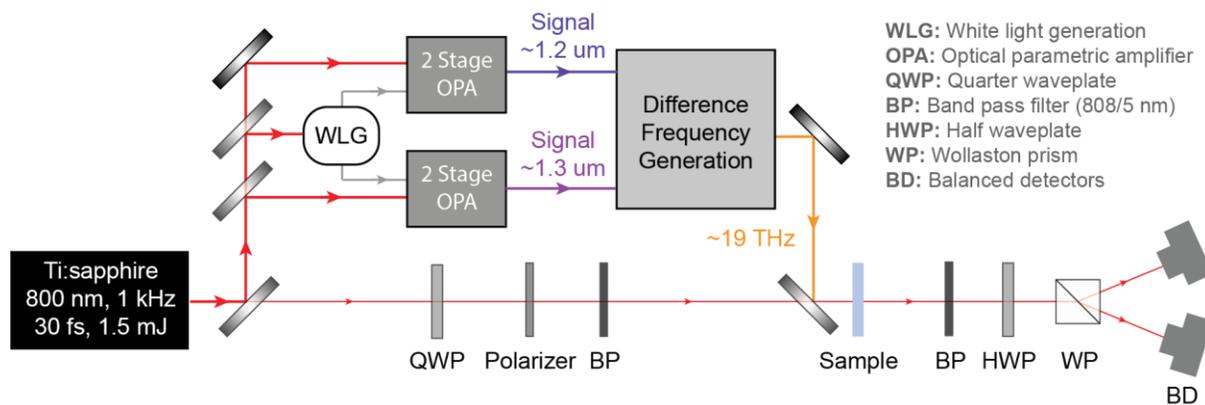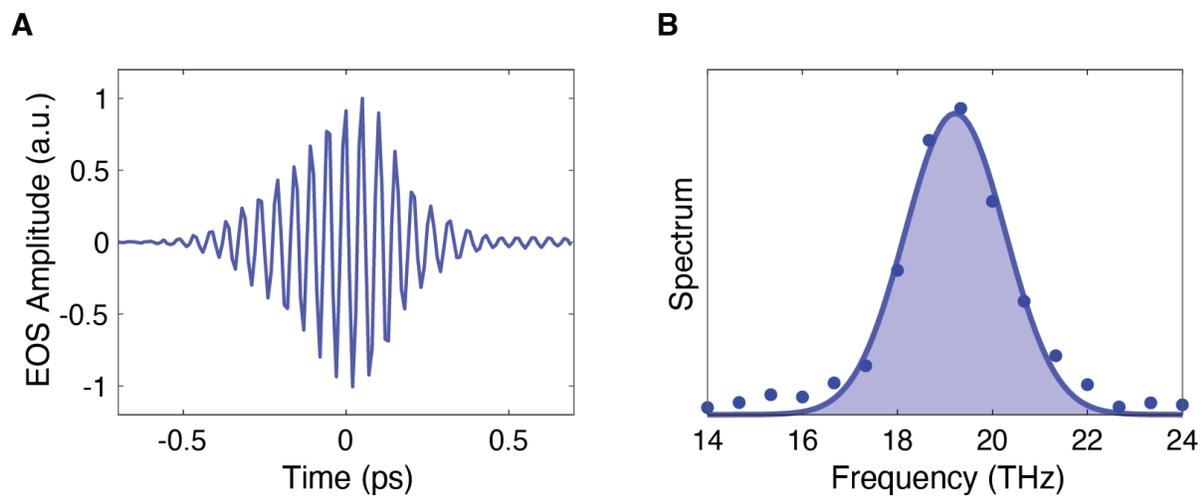
Fig. S1. Schematic of the experimental setup.

Fig. S2. Characterization of the 19-THz pump pulse. (**A**) Typical time-dependent electric field of the excitation pulses measured via electro-optic sampling (EOS). (**B**) Corresponding frequency spectrum obtained by Fourier transformation.
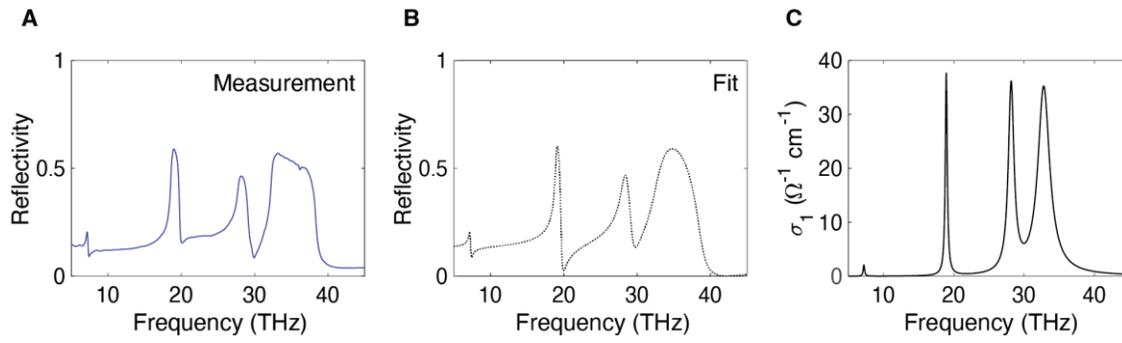
Fig. S3. Static characterization of the BPO₄ sample. (**A**) The static reflectivity spectrum of BPO₄ for electric field polarized along the *a*-axis. (**B**) Fit of the measured spectrum using the dielectric function for phonons. (**C**) Frequency dependent real part of the optical conductivity extracted from this fit.
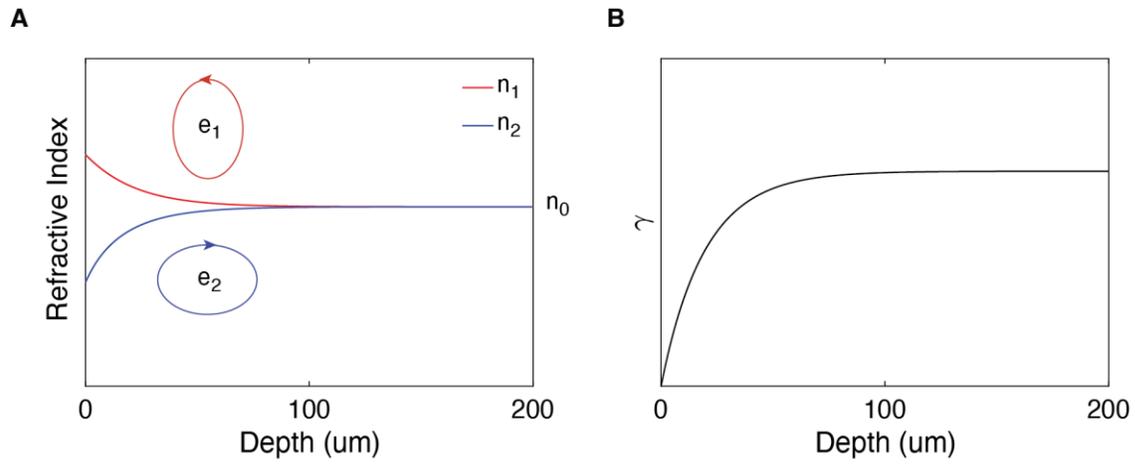
Fig. S4. Schematic of the depth-dependent light-induced polarization rotation signal.
(**A**) The refractive indices for the two elliptically polarized eigenvectors as a function of propagation depth in the BPO_4 sample. The difference between the refractive indices decreases with depth. (**B**) The accumulated phase difference as a function of the propagation depth.
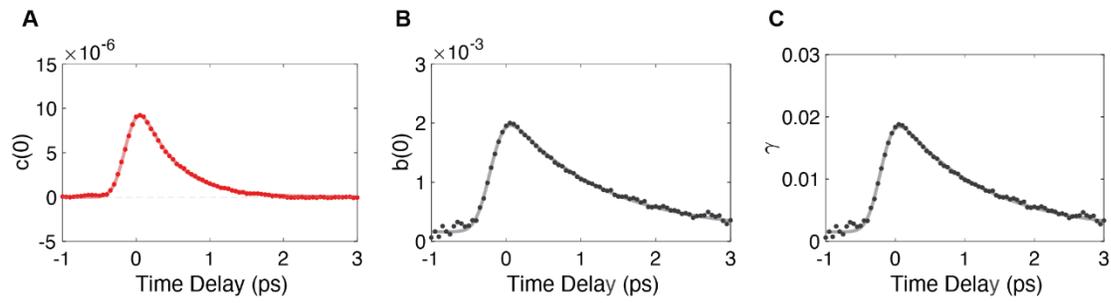
Fig. S5. Fitting results of the experimental data in Figure 3B. (**A**) Fitting result of the optical activity. (**B**) Fitting result of the birefringence. (**C**) Fitting result of the phase difference.
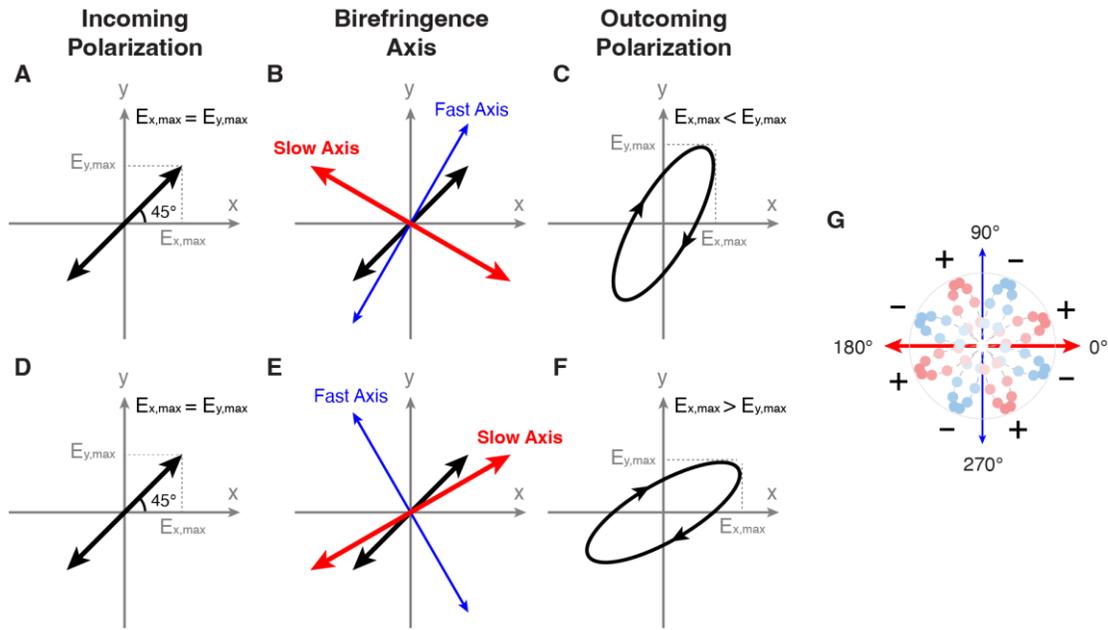
Fig. S6. Illustration of the contribution of birefringence to the polarization rotation signal. (**A**) Linearly polarized incoming polarization. X and Y axes are set to balance the signal on the two detectors. (**B**) Orientation of the birefringence axis relative to the incoming polarization with fast axis closer to the incoming polarization (**C**) The outcoming polarization, where the projections on the two detectors differ. (**D**)-(**F**) Orientation of the slow axis closer to the incoming polarization. The sign of the signal is inversed. (**G**) Polarization rotation signal as a function of the incident polarization angle.
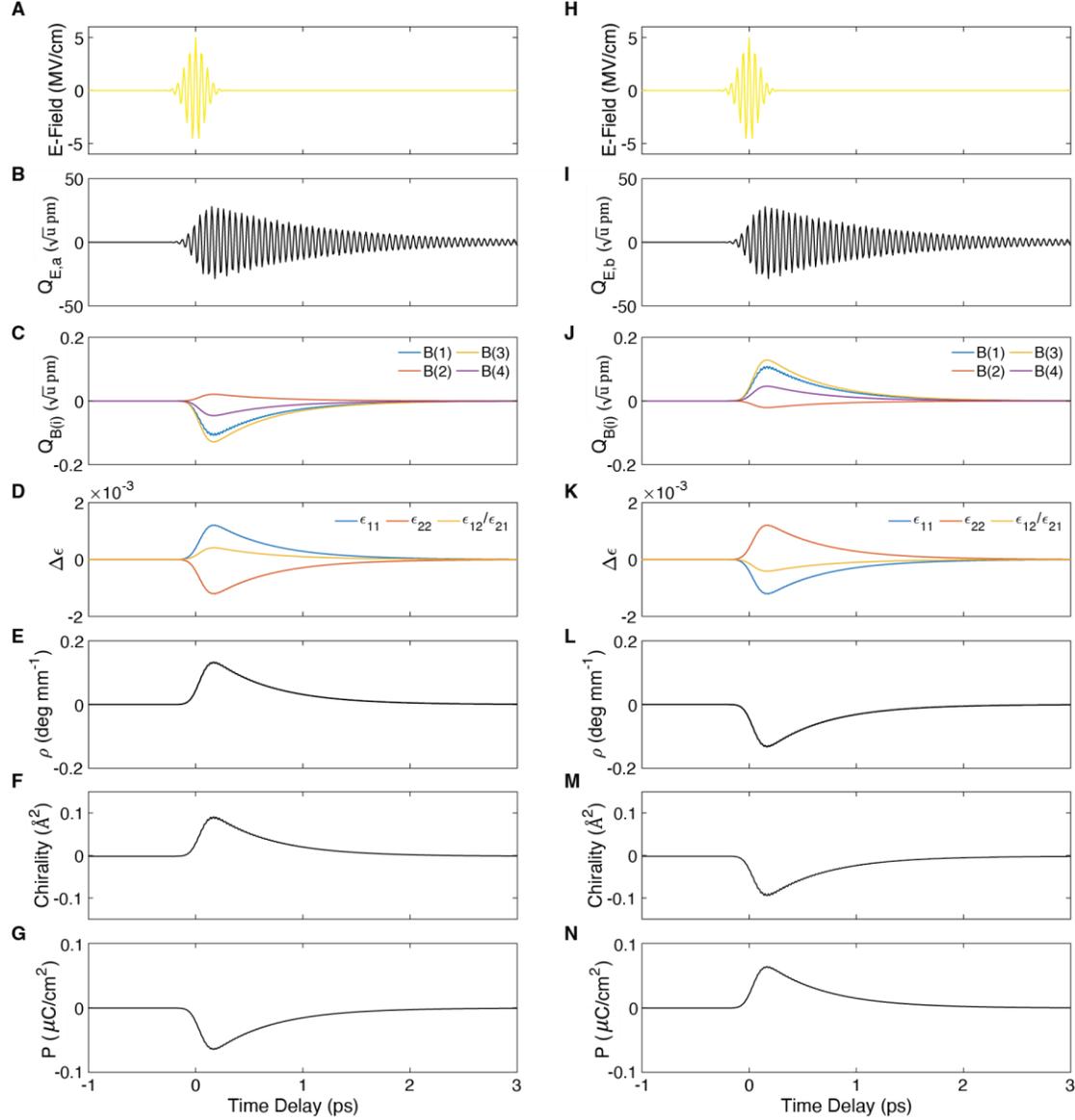
Fig. S7. Simulation of the nonlinear phonon dynamics. (**A**) The THz pump electric field. (**B**) Oscillatory motion of the driven E mode polarized along the crystal *a*-axis. (**C**) Rectified dynamics of the four nonlinearly coupled B-symmetry modes. (**D**) Changes in the optical permittivity arising from these lattice dynamics. (**E**) Temporal evolution of the rotary power. (**F**) Time-dependent chiral order parameter. (**G**) Transient c-axis polarization connected to the displaced B-symmetry modes. (**H**)-(**N**) Equivalent data set for optical excitation along the crystal *b*-axis.
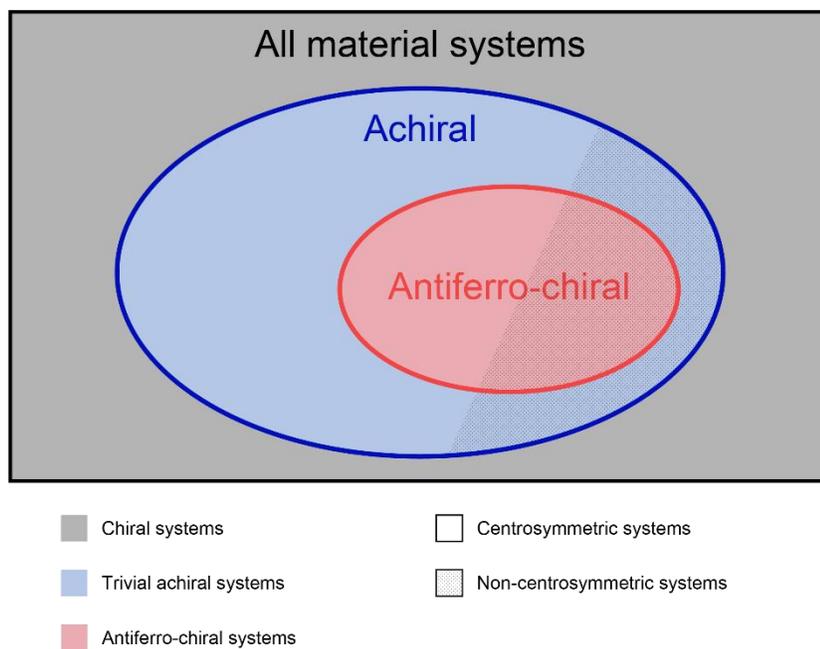
15

Fig. S8. Classification of material systems based on symmetry. Antiferro-chiral materials are a subset of achiral systems.

Table S1. Fitting results of the four E-symmetry phonon modes in BPO₄ polarized along the crystal *a* and *b* axes.

Phonon Mode	$\omega_{TO,j}$ (THz)	$\omega_{LO,j}$ (THz)	γ_j (THz)	ε_∞
E(1)	7.2	7.4	0.24	/
E(2)	18.9	20.3	0.33	/
E(3)	28.2	30.5	0.96	/
E(4)	32.8	37.0	2.0	/
/	/	/	/	2.70

Table S2. Relevant parameters of the optical phonons involved in the light-induced chiral state, obtained from DFT calculations: transverse optical frequency, nonlinear coupling coefficient, mode effective charge.

Phonon symmetry	ω_{TO} (THz)	α (meV/u$^{3/2}$Å^3)	Z^* (q$_e$/u$^{1/2}$)
E(2)	18.1	–	0.76
B(1)	15.8	1.16	0.85
B(2)	17.6	39.93	0.37
B(3)	28.1	−16.62	0.87
B(4)	31.5	105.59	1.57

Table S3. Phonon amplitude dependent changes in the dielectric tensor elements and the rotary power relevant for the light-induced chiral state, obtained from DFT calculations for the phonon modes with B-symmetry.

Phonon symmetry	$\partial\varepsilon_{11}/\partial Q_{B,i}$ $(10^3\,u^{-1/2}A^{-1})$	$\partial\varepsilon_{12}/\partial Q_{B,i}$ $(10^3\,u^{-1/2}A^{-1})$	$\partial\rho/\partial Q_{B,i}$ $(°\,mm^{-1}\,u^{-1/2}\,A^{-1})$
B(1)	31	31	-23
B(2)	33	-8	-14
B(3)	5	5	-8
B(4)	-36	-44	-60

Table S4. Phonon amplitude dependent changes in the dielectric tensor elements and the rotary power relevant for the light-induced chiral state, obtained from DFT calculations for the resonantly driven mode with E-symmetry.

Phonon symmetry	$\partial^2\varepsilon_{11}/\partial Q_{E,i}^2$ $(10^3\,u^{-1}A^{-2})$	$\partial^2\varepsilon_{12}/\partial Q_{E,i}^2$ $(10^3\,u^{-1}A^{-2})$	$\partial^2\rho/\partial Q_{E,i}^2$ $(°\,mm^{-1}\,u^{-1}A^{-2})$
E(2)	0.03	0.009	1

Table S5. Irreducible representations that induce chirality in the 21 achiral crystalline point groups.

Non-centrosymmetric Achiral Point group	Irreps	Centrosymmetric Achiral Point group	Irreps
m	A''	-1	A_u
mm2	A_2	-3	A_u, E_u
4mm	A_2, E	2/m	A_u
3m	A_2, E	4/m	A_u
6mm	A_2, E_1, E_2	6/m	A_u, E_{2u}
-42m	A_2, B_1, E	mmm	A_u
-6m2	A_1'', E''	4/mmm	A_{1u}
-43m	A_2, E, T_1, T_2	-3m	A_{1u}, E_u
-4	B, E	6/mmm	A_{1u}, E_{2u}
-6	A'', E''	m-3	A_u, E_u, T_u
		m-3m	$A_{1u}, E_u, T_{1u}, T_{2u}$

References and Notes

1. B. L. Feringa, R. A. Van Delden, Absolute asymmetric synthesis: The origin, control, and amplification of chirality. *Angew. Chem. Int. Ed.* **38**, 3418–3438 (1999). doi:10.1002/(SICI)1521-3773(19991203)38:23<3418:AID-ANIE3418>3.0.CO;2-V Medline

2. Y. Le Page, G. Donnay, Refinement of the crystal structure of low-quartz. *Acta Crystallogr. B* **32**, 2456–2459 (1976). doi:10.1107/S0567740876007966

3. T. Matsuura, H. Koshima, Introduction to chiral crystallization of achiral organic compounds: Spontaneous generation of chirality. *J. Photochem. Photobiol. Photochem. Rev.* **6**, 7–24 (2005). doi:10.1016/j.jphotochemrev.2005.02.002

4. N. Kumar, S. N. Guin, K. Manna, C. Shekhar, C. Felser, Topological quantum materials from the viewpoint of chemistry. *Chem. Rev.* **121**, 2780–2815 (2021). doi:10.1021/acs.chemrev.0c00732 Medline

5. Y. Wang, Y.-X. Li, L. Cseh, Y.-X. Chen, S.-G. Yang, X. Zeng, F. Liu, W. Hu, G. Ungar, Enantiomers self-sort into separate counter-twisted ribbons of the *Fddd* liquid crystal: Antiferrochirality and parachirality. *J. Am. Chem. Soc.* **145**, 17443–17460 (2023). doi:10.1021/jacs.3c06164 Medline

6. T. O. Yeates, S. B. Kent, Racemic protein crystallography. *Annu. Rev. Biophys.* **41**, 41–61 (2012). doi:10.1146/annurev-biophys-050511-102333 Medline

7. Z. Li, Z. Lin, Y. Wu, P. Fu, Z. Wang, C. Chen, Crystal growth, optical properties measurement, and theoretical calculation of BPO4. *Chem. Mater.* **16**, 2906–2908 (2004). doi:10.1021/cm040121o

8. C. P. Romao, D. M. Juraschek, Phonon-induced geometric chirality. *ACS Nano* **18**, 29550–29557 (2024). doi:10.1021/acsnano.4c05978 Medline

9. M. Först, C. Manzoni, S. Kaiser, Y. Tomioka, Y. Tokura, R. Merlin, A. Cavalleri, Nonlinear phononics as an ultrafast route to lattice control. *Nat. Phys.* **7**, 854–856 (2011). doi:10.1038/nphys2055

10. P. G. Radaelli, Breaking symmetry with light: Ultrafast ferroelectricity and magnetism from three-phonon coupling. *Phys. Rev. B* **97**, 085145 (2018). doi:10.1103/PhysRevB.97.085145

11. X. Li, T. Qiu, J. Zhang, E. Baldini, J. Lu, A. M. Rappe, K. A. Nelson, Terahertz field-induced ferroelectricity in quantum paraelectric $SrTiO_3$. *Science* **364**, 1079–1082 (2019). doi:10.1126/science.aaw4913 Medline

12. A. Stupakiewicz, C. S. Davies, K. Szerenos, D. Afanasiev, K. S. Rabinovich, A. V. Boris, A. Caviglia, A. V. Kimel, A. Kirilyuk, Ultrafast phononic switching of magnetization. *Nat. Phys.* **17**, 489–492 (2021). doi:10.1038/s41567-020-01124-9

13. A. S. Disa, T. F. Nova, A. Cavalleri, Engineering crystal structures with light. *Nat. Phys.* **17**, 1087–1092 (2021). doi:10.1038/s41567-021-01366-1

14. J. Luo, T. Lin, J. Zhang, X. Chen, E. R. Blackert, R. Xu, B. I. Yakobson, H. Zhu, Large effective magnetic fields from chiral phonons in rare-earth halides. *Science* **382**, 698–702 (2023). doi:10.1126/science.adi9601 Medline

15. M. Fechner, M. Först, G. Orenstein, V. Krapivin, A. S. Disa, M. Buzzi, A. von Hoegen, G. de la Pena, Q. L. Nguyen, R. Mankowsky, M. Sander, H. Lemke, Y. Deng, M. Trigo, A. Cavalleri, Quenched lattice fluctuations in optically driven $SrTiO_3$. *Nat. Mater.* **23**, 363–368 (2024). [doi:10.1038/s41563-023-01791-y](doi:10.1038/s41563-023-01791-y) Medline

16. M. Basini, M. Pancaldi, B. Wehinger, M. Udina, V. Unikandanunni, T. Tadano, M. C. Hoffmann, A. V. Balatsky, S. Bonetti, Terahertz electric-field-driven dynamical multiferroicity in $SrTiO_3$. *Nature* **628**, 534–539 (2024). [doi:10.1038/s41586-024-07175-9](doi:10.1038/s41586-024-07175-9) Medline

17. C. S. Davies, F. G. N. Fennema, A. Tsukamoto, I. Razdolski, A. V. Kimel, A. Kirilyuk, Phononic switching of magnetization by the ultrafast Barnett effect. *Nature* **628**, 540–544 (2024). [doi:10.1038/s41586-024-07200-x](doi:10.1038/s41586-024-07200-x) Medline

18. D. Fausti, R. I. Tobey, N. Dean, S. Kaiser, A. Dienst, M. C. Hoffmann, S. Pyon, T. Takayama, H. Takagi, A. Cavalleri, Light-induced superconductivity in a stripe-ordered cuprate. *Science* **331**, 189–191 (2011). doi:10.1126/science.1197294 Medline

19. R. Mankowsky, A. Subedi, M. Först, S. O. Mariager, M. Chollet, H. T. Lemke, J. S. Robinson, J. M. Glownia, M. P. Minitti, A. Frano, M. Fechner, N. A. Spaldin, T. Loew, B. Keimer, A. Georges, A. Cavalleri, Nonlinear lattice dynamics as a basis for enhanced superconductivity in YBa2Cu3O6.5. *Nature* **516**, 71–73 (2014). doi:10.1038/nature13875 Medline

20. R. Mankowsky, A. von Hoegen, M. Först, A. Cavalleri, Ultrafast reversal of the ferroelectric polarization. *Phys. Rev. Lett.* **118**, 197601 (2017). doi:10.1103/PhysRevLett.118.197601 Medline

21. T. F. Nova, A. S. Disa, M. Fechner, A. Cavalleri, Metastable ferroelectricity in optically strained $SrTiO_3$. *Science* **364**, 1075–1079 (2019). doi:10.1126/science.aaw4911 Medline

22. A. S. Disa, M. Fechner, T. F. Nova, B. Liu, M. Först, D. Prabhakaran, P. G. Radaelli, A. Cavalleri, Polarizing an antiferromagnet by optical engineering of the crystal field. *Nat. Phys.* **16**, 937–941 (2020). [doi:10.1038/s41567-020-0936-3](doi:10.1038/s41567-020-0936-3)

23. Materials, methods, and additional information are available in the supplementary materials.

24. R. Oiwa, H. Kusunose, Rotation, electric-field responses, and absolute enantioselection in chiral crystals. *Phys. Rev. Lett.* **129**, 116401 (2022). doi:10.1103/PhysRevLett.129.116401 Medline

25. G. H. Fecher, J. Kübler, C. Felser, Chirality in the solid state: Chiral crystal structures in chiral and achiral space groups. *Materials* **15**, 5812 (2022). [doi:10.3390/ma15175812](doi:10.3390/ma15175812) Medline

26. F. Arago, *Sur une modification remarquable qu'éprouvent les rayons lumineux dans leur passage à travers certains corps diaphanes, et sur quelques autres nouveaux phénomènes d'optiques: Lu le 11 août 1811* (Firmin-Didot, 1812).

27. J.-B. Biot, *Mémoire sur un nouveau genre d'oscillation que les molécules de la lumiere éprouvent en traversant certains cristaux* (Chez Firmin Didot, 1814).

28. C. Rockstuhl, C. Menzel, T. Paul, F. Lederer, Optical activity in chiral media composed of three-dimensional metallic meta-atoms. *Phys. Rev. B Condens. Matter Mater. Phys.* **79**, 035321 (2009). doi:10.1103/PhysRevB.79.035321

29. M. Kuwata-Gonokami, N. Saito, Y. Ino, M. Kauranen, K. Jefimovs, T. Vallius, J. Turunen, Y. Svirko, Giant optical activity in quasi-two-dimensional planar nanostructures. *Phys. Rev. Lett.* **95**, 227401 (2005). doi:10.1103/PhysRevLett.95.227401 Medline

30. M. De Vido, K. Ertel, A. Wojtusiak, P. D. Mason, P. J. Phillips, S. Banerjee, J. M. Smith, T. J. Butcher, C. Edwards, Optical rotatory power of quartz between 77 K and 325 K for 1030 nm wavelength. *Opt. Mater. Express* **9**, 2708–2715 (2019). [doi:10.1364/OME.9.002708](doi:10.1364/OME.9.002708)

31. A. Zyuzin, A. Burkov, Topological response in Weyl semimetals and the chiral anomaly. *Phys. Rev. B Condens. Matter Mater. Phys.* **86**, 115133 (2012). doi:10.1103/PhysRevB.86.115133

32. H. B. Nielsen, M. Ninomiya, The Adler-Bell-Jackiw anomaly and Weyl fermions in a crystal. *Phys. Lett. B* **130**, 389–396 (1983). [doi:10.1016/0370-2693(83)91529-0](doi:10.1016/0370-2693(83)91529-0)

33. N. Ong, S. Liang, Experimental signatures of the chiral anomaly in Dirac–Weyl semimetals. *Nat. Rev. Phys.* **3**, 394–404 (2021). [doi:10.1038/s42254-021-00310-9](doi:10.1038/s42254-021-00310-9)

34. J. Ishioka, Y. H. Liu, K. Shimatake, T. Kurosawa, K. Ichimura, Y. Toda, M. Oda, S. Tanda, Chiral charge-density waves. *Phys. Rev. Lett.* **105**, 176401 (2010). doi:10.1103/PhysRevLett.105.176401 Medline

35. S.-Y. Xu, Q. Ma, Y. Gao, A. Kogar, A. Zong, A. M. Mier Valdivia, T. H. Dinh, S.-M. Huang, B. Singh, C.-H. Hsu, T.-R. Chang, J. P. C. Ruff, K. Watanabe, T. Taniguchi, H. Lin, G. Karapetrov, D. Xiao, P. Jarillo-Herrero, N. Gedik, Spontaneous gyrotropic electronic order in a transition-metal dichalcogenide. *Nature* **578**, 545–549 (2020). [doi:10.1038/s41586-020-2011-8](doi:10.1038/s41586-020-2011-8) Medline

36. C. Manzoni, M. Först, H. Ehrke, A. Cavalleri, Single-shot detection and direct control of carrier phase drift of midinfrared pulses. *Opt. Lett.* **35**, 757–759 (2010). [doi:10.1364/OL.35.000757](doi:10.1364/OL.35.000757) Medline

37. P. J. Moll, Focused ion beam microstructuring of quantum matter. *Annu. Rev. Condens. Matter Phys.* **9**, 147–162 (2018). doi:10.1146/annurev-conmatphys-033117-054021

38. A. Barker Jr., Temperature dependence of the transverse and longitudinal optic mode frequencies and charges in $SrTiO_3$ and $BaTiO_3$. *Phys. Rev.* **145**, 391–399 (1966). doi:10.1103/PhysRev.145.391

39. R. C. Jones, A new calculus for the treatment of optical systemsi. description and discussion of the calculus. *J. Opt. Soc. Am.* **31**, 488–493 (1941). doi:10.1364/JOSA.31.000488

40. G. Kresse, J. Furthmüller, Efficiency of ab-initio total energy calculations for metals and semiconductors using a plane-wave basis set. *Comput. Mater. Sci.* **6**, 15–50 (1996). [doi:10.1016/0927-0256(96)00008-0](doi:10.1016/0927-0256(96)00008-0)

41. G. Kresse, J. Hafner, Ab initio molecular dynamics for liquid metals. *Phys. Rev. B Condens. Matter* **47**, 558–561 (1993). doi:10.1103/PhysRevB.47.558 Medline

42. G. Kresse, J. Furthmüller, Efficient iterative schemes for ab initio total-energy calculations using a plane-wave basis set. *Phys. Rev. B Condens. Matter* **54**, 11169–11186 (1996). doi:10.1103/PhysRevB.54.11169 Medline

43. A. Togo, First-principles phonon calculations with phonopy and phono3py. *J. Phys. Soc. Jpn.* **92**, 012001 (2023). doi:10.7566/JPSJ.92.012001

44. G. Kresse, D. Joubert, From ultrasoft pseudopotentials to the projector augmented-wave method. *Phys. Rev. B Condens. Matter* **59**, 1758–1775 (1999). doi:10.1103/PhysRevB.59.1758

45. H. J. Monkhorst, J. D. Pack, Special points for Brillouin-zone integrations. *Phys. Rev., B, Solid State* **13**, 5188–5192 (1976). doi:10.1103/PhysRevB.13.5188

46. X. Gonze, C. Lee, Dynamical matrices, Born effective charges, dielectric permittivity tensors, and interatomic force constants from density-functional perturbation theory. *Phys. Rev. B Condens. Matter* **55**, 10355–10368 (1997). doi:10.1103/PhysRevB.55.10355

47. X. Wang, Y. Yan, Optical activity of solids from first principles. *Phys. Rev. B* **107**, 045201 (2023). doi:10.1103/PhysRevB.107.045201

48. A. Inda, R. Oiwa, S. Hayami, H. M. Yamamoto, H. Kusunose, Quantification of chirality based on electric toroidal monopole. *J. Chem. Phys.* **160**, 184117 (2024). [doi:10.1063/5.0204254](doi:10.1063/5.0204254) Medline